Appendix B

Code verification

We demonstrate the accuracy of the pseudo-spectral spatio-temporal numerical scheme using a number of tests. Before delving into the verification details, it is important to understand the parameter regimes of the waves and the limiting factors controlling the simulation timestep. The highest frequency of waves of interest to us are of the order of 6 mHz, corresponding to a timescale of about 167 seconds. The simulation timesteps - 4 seconds for the spherical calculations and 2 seconds for the Cartesian case, are significantly smaller than the period of the oscillations. The calculations are evidently temporally highly over resolved; compared to the 4-10 points per wavelength (ppw) quoted by Hu et al. (1996) and Berland et al. (2006), the simulations operate at between 40-80 ppw. Similarly, as shown in Figure B.1, radial resolution is quite sufficient. In fact, the eigenfunctions of the modes contain a rather small number of nodes (10 - 30 depending on the mode) in comparison to the actual number of grid points. The reason for the excessive spatial resolution is the need to capture the rapid density (pressure) variation with radius. Therefore, the limiting factor in terms of the timestep or CFL number is the large number of density (pressure) scale heights in the computational domain, which is why the spatial and temporal resolutions are so high.

Having stated this, it is important to demonstrate that we are indeed in a high-accuracy regime. Firstly, we demonstrate in Figure B.2 that the boundary conditions cause the error convergence rate of the compact finite differences to drop to fifth

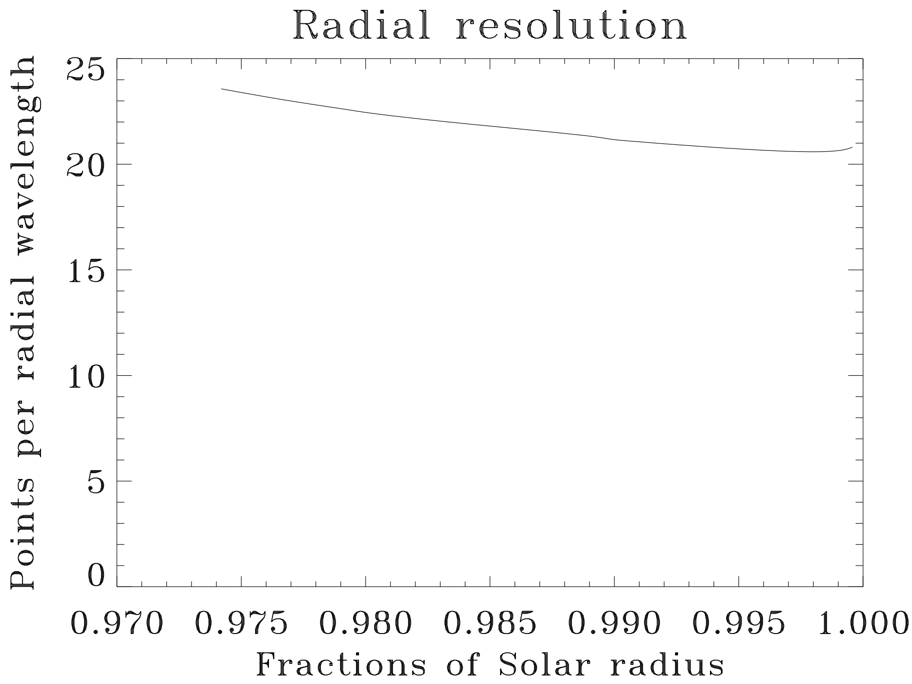

Figure B.1 Resolution in the radial direction as a function of the non-dimensional radius; the solid line shows the grid spacing of the simulation. The wavelength in the radial direction is calculated from equation 2.7. We only display the grid spacing of a small fraction of the solar model, which actually extends from $r = 0.2R_\odot$ to $1.002R_\odot$ ($n_{rad} = 400$). The wavelength becomes a non-trivial fraction of the solar radius by about $r = 0.8R_\odot$, and the resolution monotonically increases with decreasing radius.

order. Although not shown here, the convergence rate is entirely unchanged when the radial de-aliasing filter, described in § 2.5.2, is applied in conjunction with the finite differences. Next, to demonstrate the accuracy of the spatial scheme in its entirety (i.e., when used with radial de-aliasing and the temporal scheme), we simulate the 1-D propagation of a Gaussian wavelet in a box with reflecting boundary conditions. The grid-spacing in the calculation follows the constant travel-time criterion developed in § 2.5.1. The background model is chosen to be an adiabatically stratified, truncated polytrope with index $m = 1.5$, gravity $\mathbf{g} = -2.775 \times 10^4$ cm s$^{-2}\mathbf{e_z}$, reference pressure $p_{ref} = 1.21 \times 10^5$ g cm^{-1} s^{-2} and reference density $\rho_{ref} = 2.78 \times 10^{-7}$ g cm^{-3}, such that the pressure and density variations are given by,

$$p_0(z) = p_{ref} \left(-\frac{z}{z_0}\right)^{m+1}, \tag{B.1}$$

and

$$\rho_0(z) = \rho_{ref} \left(-\frac{z}{z_0}\right)^{m}. \tag{B.2}$$

The photospheric level of the background model is at $z = 0$, with the upper boundary placed at a depth of $z_0 = 768$ km. This model is similar to the stratification prevalent in the outer layers of the Sun (e.g., Bogdan et al., 1996). Because error convergence rates are very sensitive and easily masked by small errors such as the locations of the comparison points of solutions, we start with a highly resolved 721 point grid and downsample by successively higher rates (every second point, every third point, and so on). The solutions obtained on this sequence of grids are compared with the highly resolved case to obtain the error convergence rate. The lower boundary of the simulation is placed at $z = -20.876$ Mm, with wall-like boundary conditions on both ends ($v = 0, \partial_z p = -\rho g$, at the boundaries). The timestep of the simulation was chosen to be $\Delta t = 0.05$ seconds. The experiment is graphically displayed in Figure B.3 and the error convergence rate is shown in Figure B.4.

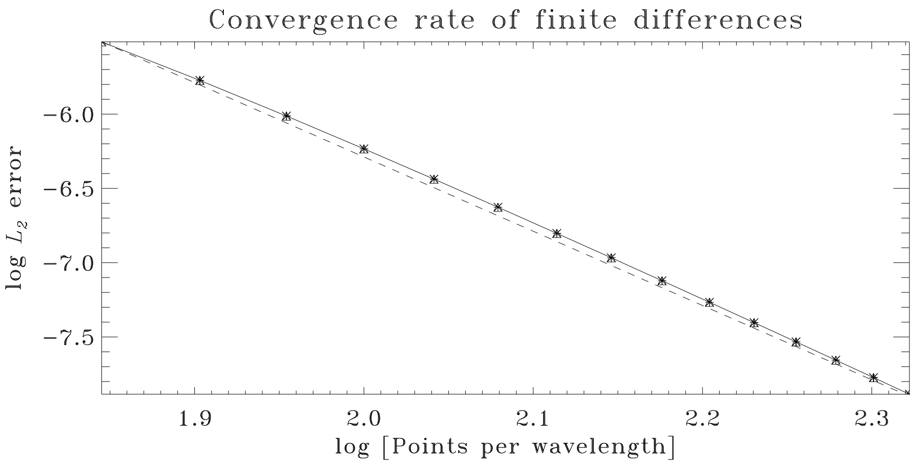

Figure B.2 Spatial convergence rate of the compact finite differences with fifth-order accurate boundary conditions. The solid line shows the accuracy of the scheme, while the dashed line is the theoretical fifth-order accuracy curve.

B.0.1 Eigenfunctions

For the polytrope described above, it is possible to determine the eigenfunctions analytically (e.g., Bogdan & Cally, 1995). This will assist us in verifying that the spatial scheme is able to recover the eigenfunctions accurately. The first step is to set down the equations to be solved:

$$\partial_t \rho(z,t) = -\partial_z(\rho_0 v) \tag{B.3}$$

$$\rho_0 \partial_t v(z,t) = -\partial_z p - \rho g \tag{B.4}$$

$$\partial_t p(z,t) = -c_0^2 \rho_0 \partial_z v + \rho_0 v g, \tag{B.5}$$

where ρ refers to density, c refers to sound speed, the 0 subscript refers to background properties of the model, z is the spatial coordinate and t time. Differentiating equation (B.4) with respect to time and substituting for time derivatives of density and pressure from equations (B.3) and (B.5) respectively, we obtain the following:

$$\rho_0 \partial_t^2 v(z,t) = -\partial_z(-c_0^2 \rho_0 \partial_z v + \rho_0 v g) + \partial_z(\rho_0 g v). \tag{B.6}$$

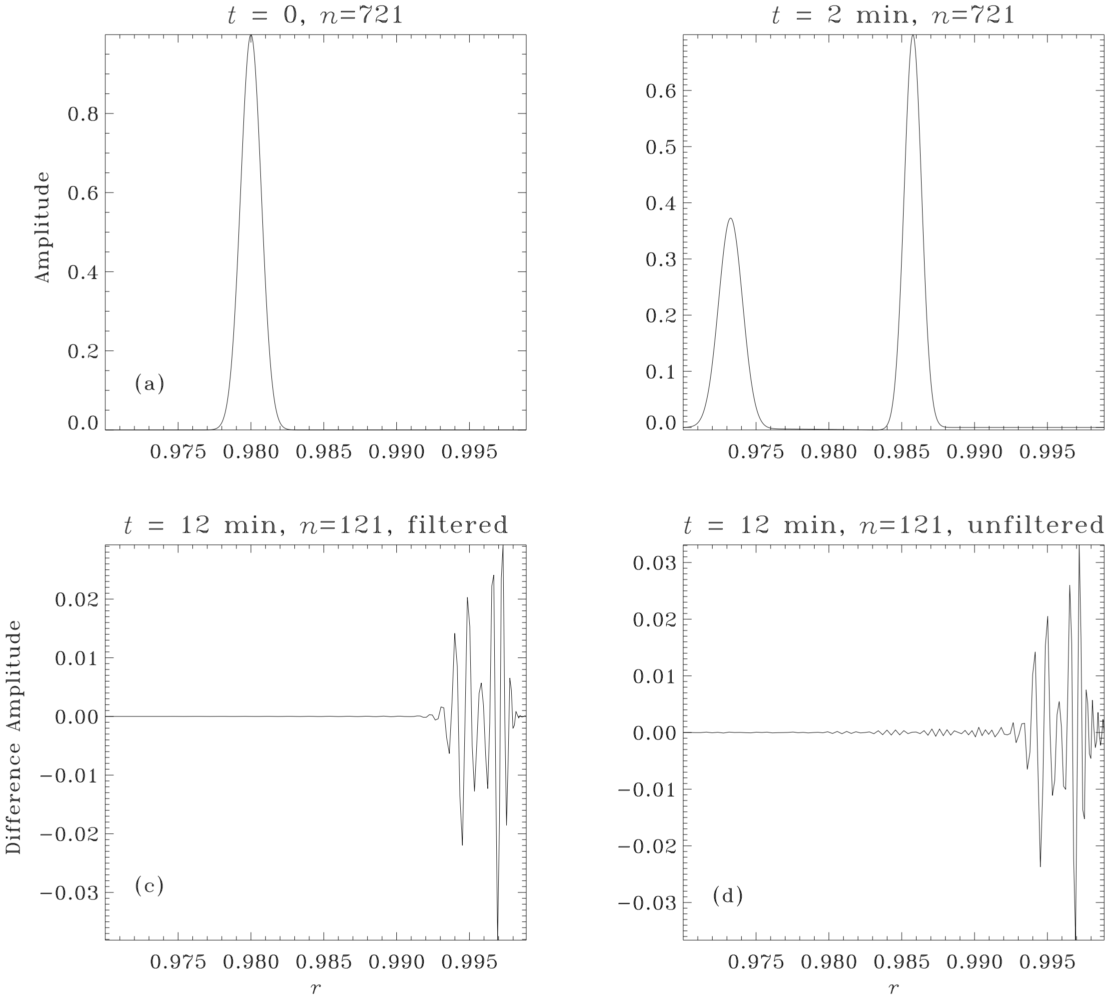

Figure B.3 Experiment to determine the spatial error convergence rate. The initial condition, a Gaussian wavelet in velocity, is shown in panel (a). In (b), the temporally evolved wavelet at time $t = 2$ min is displayed. Simulations are performed with varying numbers of grid points, $n = 721, 361, 181, 145$, and 121, so that each grid is a downsampled version (i.e., every other point, every third point etc.) of the $n = 721$ case. Errors are computed at $t = 2$ min using a downsampled version of the $n = 721, t = 2$ min solution as a template (panel b). In panels (c) and (d), the differences between the $n = 121$ solution and the downsampled $n = 721$ template at $t = 12$ min are displayed; it is seen that the difference, interpreted as the error, is greater in the unfiltered case in panel (d) than in the filtered version in panel (c), where the filter is applied to dealias variables in the radial direction (§ 2.5.2). The difference between (c) and (d), which although appears harmless, continues to grow, eventually overwhelming the simulation unless a de-aliasing filter is applied frequently.

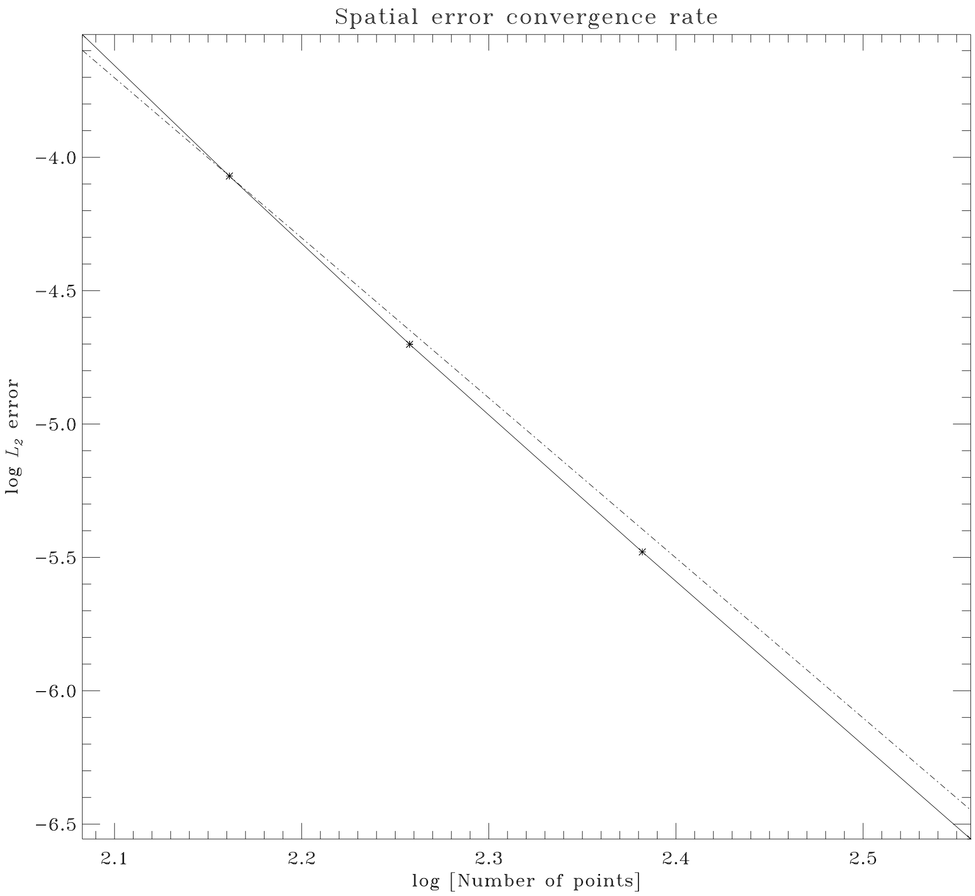

Figure B.4 Spatial error convergence rate (with radial dealiasing) based on the experiment of Figure B.3; the time step was $\Delta t = 0.05$ seconds. The solid line is the error of the compact finite differences and the dashed line is a theoretical sixth-order accuracy accuracy curve. It is somewhat surprising that the scheme obeys a sixth-order accuracy law despite the use of fifth-order boundary conditions. Partly, the reason could be that the problem is a consistent initial-boundary value problem, i.e. $v = 0$ and $\partial_z p = -\rho g$ at the boundaries.

Next we define the Eulerian pressure and velocity fluctuations to be, respectively:

$$
\begin{aligned}
p(z,t) &= \int_{-\infty}^{\infty} d\omega \tilde{P}(z,\omega) e^{-i\omega t} && \text{(B.7)}\\
v(z,t) &= \int_{-\infty}^{\infty} d\omega \tilde{V}(z,\omega) e^{-i\omega t}, && \text{(B.8)}
\end{aligned}
$$

where,

$$
\begin{aligned}
\tilde{P}(z,\omega) &= e^{-\frac{(\omega-\omega_0)^2}{2\Omega^2}} p^*(z,\omega), && \text{(B.9)}\\
\tilde{V}(z,\omega) &= e^{-\frac{(\omega-\omega_0)^2}{2\Omega^2}} v^*(z,\omega). && \text{(B.10)}
\end{aligned}
$$

Substituting these expressions into equation (B.6), we have:

$$-\omega^2 \rho_0 z_0^2 v^* = \partial_s (c_0^2 \rho_0 \partial_s v^*), \tag{B.11}$$

where once again, $s = -z/z_0$, $\rho_0 = \rho_c s^m$, $p_0 = p_c s^{m+1}$, $c_0^2 = \tilde{c^2} s$, and $\rho_c, p_c, \tilde{c^2}$ are the density, pressure and sound speed square at $s = 1$. Equation (B.11) is simplified to obtain:

$$s\partial_s^2 v^* + (m+1)\partial_s v^* + \frac{\alpha^2}{4} v^* = 0, \tag{B.12}$$

where $\alpha = 2\omega z_0/\tilde{c}$. Equation (B.12) is solved to obtain the analytical expression for the eigenfunction:

$$v^* = A s^{-m/2} J_m(\alpha s^{1/2}) + B s^{-m/2} Y_m(\alpha s^{1/2}). \tag{B.13}$$

The constants A and B are determined by enforcing the boundary conditions $v^*(s = 1) = 0$ and $v^*(s = D) = 0$. From these conditions emerge a sequence of resonant frequencies, α, which can then be used to obtain the eigenfunctions of the resonant modes. The eigenfunction for pressure is related to the one for velocity according to:

$$
\begin{aligned}
p^* &= \frac{i}{\omega}\left[\rho_0 v^* g + \frac{c_0^2 \rho_0}{z_0} \partial_s v^*\right] && \text{(B.14)}\\
p^* &= \frac{2i\rho_c \tilde{c}}{\alpha} s^m [m v^* + s\partial_s v^*]. && \text{(B.15)}
\end{aligned}
$$

To obtain eigenfunctions from the calculations, we first excite and simulate wave propagation in the above-described cavity. Temporal transforms of the entire dataset are computed at each spatial location; resonant modes are then isolated by analyzing large amplitude regions in the power spectrum. These frequencies are compared to the analytically predicted values to ensure that these are indeed resonant modes. Having done so, the temporal spectrum is multiplied by a frequency-window function to retain power only in the region of interest and inverse Fourier transformed. The spatial extent of the eigenfunction of interest is then observed at temporal points that correspond closely to the period of the mode. However, spatial error convergence rates are difficult to measure from this experiment because the eigenfunction signal is diluted by neighbouring modes due to the finite temporal window of the simulations. Moreover the accuracy with which the resonant frequency can be measured is bounded by the time length of the calculation. For the eigenfunction shown in Figure B.5, a resonant mode with $\nu = 6.6111$ mHz was isolated using an extremely narrow, four-point box-car type frequency filter. Simulations with varying grid spacings all showed a peak in the power spectrum at frequency of 9 μHz away from the analytical prediction (frequency resolution $\sim 22\mu$Hz, from a 12-hour simulation).

B.0.2 Efficacy of the transmitting boundary

As described in § 2.2, we use the transmitting boundary conditions of Thompson (1990) with an adjoining sponge (e.g., Lui, 2003) to 'prepare' the waves for the boundary. The main reason for using this prescription as opposed to other possibilities (Giles (1990); Poinsot & Lele (1992); see Colonius (2004) for a review) is the ease of implementation and efficiency of the method.

To test if these boundary conditions change the eigenfunction in any significant manner and to ensure that to large extent, they are indeed non reflecting, we perform 1D calculations of wave propagation through a background similar to that of § B.0.1. Tests of eigenfunctions corresponding to the full 3D spherical case are made difficult by the lack of analytical solutions, especially for those corresponding high-l, high frequency wave modes. Moreover, since ADIPACK allows a specific set of boundary

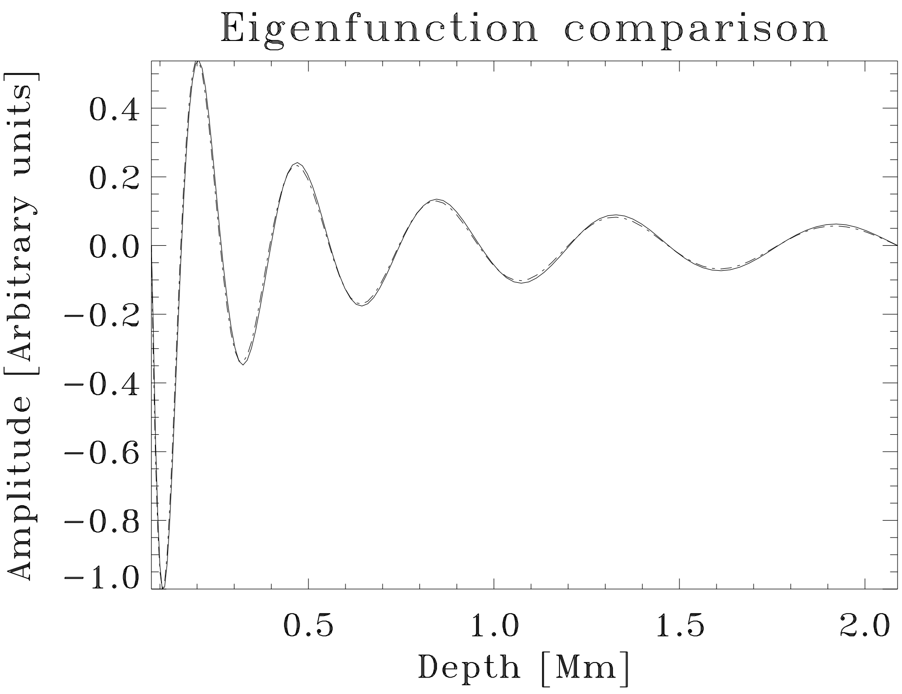

Figure B.5 Comparison of eigenfunctions for a resonant mode of frequency $\nu = 6.6111$ mHz, obtained analytically (solid line) and through simulation (dot-dash line) with $n = 121$. At higher resolutions, the two curves are virtually indistinguishable and hence are not shown here. Including the two boundaries, the eigenfunction contains only eleven nodes, far smaller than the number of grid points. With fewer ($\lesssim 80$) points, the system develops instabilities because of the steep density gradient.

condition options (different from the ones implemented in § 2.2), we are unable to place bounds on the error in capturing these modes in simulations that use a solar-like model as the background state in conjunction with the sponge.

However, in the 1-D situation discussed above, we give the problem a realistic spin by stitching an isothermal atmosphere to the polytrope so that the acoustic cut-off frequency is raised, providing a natural reflection region for the waves. Moreover, having computed the eigenfunctions of the interior (Eq.[B.13]), we relax the zero-velocity condition on the upper boundary while still enforcing a zero-velocity condition on the lower boundary. Waves whose frequencies are lower than the acoustic cutoff are reflected back into the interior while an evanescent non-propagating region develops in the isothermal atmosphere. Thus, we can determine the effect of the boundary conditions on the simulated eigenfunctions by comparing them with their analytical counterparts.

B.0.3 Evanescent behaviour

Let us assume an isothermal evanescent region with constant sound-speed c_0 with exponentially decaying density and pressure profiles:

$$\rho_e = \rho_c e^{-(z_0+z)/H}, \tag{B.16}$$

$$p_e = p_c e^{-(z_0+z)/H}, \tag{B.17}$$

$$T_e = T_c, \tag{B.18}$$

with $x = 0$ corresponding to the 'photosphere' of this model, and H to the scale height in the atmosphere. Differentiating equation (B.4) w.r.t. time and substituting for time derivatives of density and pressure from equations (B.3) and (B.5),

$$\rho_e \partial_t^2 v = -\partial_z \left[\rho_e g v - c_0^2 \rho_e \partial_z v\right] + \partial_z(\rho_e g') \tag{B.19}$$

$$-\omega^2 v = \frac{c_0^2}{\rho_e}(\partial_z \rho_e)(\partial_z v) + c_0^2 \partial_z^2 v. \tag{B.20}$$

(B.21)

Again, we define $v(z,t), p(z,t)$ as:

$$p(z,t) = \int_{-\infty}^{\infty} d\omega \tilde{P}_e(\omega,t) e^{-i\omega t} \tag{B.22}$$

$$v(z,t) = \int_{-\infty}^{\infty} d\omega \tilde{V}_e(\omega,t) e^{-i\omega t}, \tag{B.23}$$

$$\tag{B.24}$$

where $\tilde{P}_e(\omega,t)$ and $\tilde{V}_e(\omega,t)$ are given by

$$\tilde{P}_e(\omega,t) = e^{-\frac{(\omega-\omega_0)^2}{2\Omega^2}} p_e^*(\omega,z) \tag{B.25}$$

$$\tilde{V}_e(\omega,t) = e^{-\frac{(\omega-\omega_0)^2}{2\Omega^2}} v_e^*(\omega,z) \tag{B.26}$$

$$p_e^* = Be^{\lambda z - z/H} \tag{B.27}$$

$$v_e^* = Be^{\lambda z} \tag{B.28}$$

we obtain the following solution for λ,

$$\lambda^2 - \frac{\lambda}{H} + \frac{\omega^2}{c_0^2} = 0 \tag{B.29}$$

$$\lambda = \frac{1}{2H}\left[1 - \sqrt{1 - \frac{\omega^2}{\omega_a^2}}\right] \tag{B.30}$$

$$\omega_a = \frac{c_0}{2H} \tag{B.31}$$

We obtain two solutions while determining λ, and we reject the solution whose energy density $\propto \rho v^2$ grows without bound. In this situation, the relation between $\tilde{P}_e(\omega,t)$ and $\tilde{V}_e(\omega,t)$ is given by:

$$\tilde{V}_e(\omega,t) = \frac{i\omega}{\rho_c \eta} \tilde{P}_e(\omega,t) \tag{B.32}$$

$$\eta = c_0^2 \lambda - g. \tag{B.33}$$

For boundary conditions, we use normal velocity and Eulerian pressure matching across the boundary:

$$
\begin{aligned}
v^* &= v_e^* && \text{(B.34)}\\
p^* + \frac{\rho_c g}{i\omega} v^* &= p_e^* + \frac{\rho_c g}{i\omega} v_e^* && \text{(B.35)}\\
p^* &= p_e^*. && \text{(B.36)}
\end{aligned}
$$

When writing the velocities in the following form, we will have only the pressure equation to solve:

$$
\begin{aligned}
v^* &= A\frac{i\omega}{\rho_c \eta} e^{-\lambda z_0} s^{-m/2} [J_m(\alpha s^{1/2}) + \beta Y_m(\alpha s^{1/2})] && \text{(B.37)}\\
v_e^* &= A\frac{i\omega}{\rho_c \eta} e^{-\lambda s z_0} [J_m(\alpha) + \beta Y_m(\alpha)], && \text{(B.38)}\\
p_e^* &= A e^{-\lambda s z_0 + s z_0/H} [J_m(\alpha) + \beta Y_m(\alpha)], && \text{(B.39)}\\
& && \text{(B.40)}
\end{aligned}
$$

where β, A are the unknown constants we must determine. Matching $p_e^* = p^*$ at $s = 1$ gives us the following equations:

$$
\begin{aligned}
p^* &= A e^{-\lambda z_0} \frac{2i\rho_c \tilde{c}}{\alpha} \frac{i\omega}{\rho_c \eta} \Big[m J_m(\alpha) + m\beta Y_m(\alpha) \\
&\quad + \frac{1}{2}(-m J_m(\alpha) + \alpha J_m'(\alpha)) + \frac{\beta}{2}(-m Y_m(\alpha) + \alpha Y_m'(\alpha)) \Big], && \text{(B.41)}\\
p^* &= -A e^{-\lambda z_0} \frac{\omega \tilde{c}}{\alpha \eta} \left[m J_m(\alpha) + \alpha J_m'(\alpha) + \beta(m Y_m(\alpha) + \alpha Y_m'(\alpha)) \right], && \text{(B.42)}\\
\beta &= -\left[\frac{J_m(\alpha) + \frac{\omega \tilde{c}}{\alpha \eta} e^{-z_0/H} [m J_m(\alpha) + \alpha J_m'(\alpha)]}{Y_m(\alpha) + \frac{\omega \tilde{c}}{\alpha \eta} e^{-z_0/H} [m Y_m(\alpha) + \alpha Y_m'(\alpha)]} \right], && \text{(B.43)}\\
\beta &= -\left[\frac{J_m(\alpha) + \kappa J_{m-1}(\alpha)}{Y_m(\alpha) + \kappa Y_{m-1}(\alpha)} \right], && \text{(B.44)}\\
\kappa &= \frac{\omega c_0}{\alpha \eta} e^{-z_0/H}. && \text{(B.45)}
\end{aligned}
$$

To determine the resonant modes of this model, we use the definition of β from equation (B.43) and set equation (B.37) to zero at $s = D$. Having then recovered the resonant frequencies, the corresponding expressions for pressure and velocity in the interior (pure spatial components) may be obtained by evaluating:

$$v^* = A\frac{i\kappa}{\rho_c \tilde{c}} e^{-\lambda z_0 + z_0/H} s^{-m/2} [J_m(\alpha s^{1/2}) + \beta Y_m(\alpha s^{1/2})], \tag{B.46}$$

$$p^* = -A\kappa e^{-\lambda z_0 + z_0/H} s^{(m+1)/2} [J_{m-1}(\alpha s^{1/2}) + \beta Y_{m-1}(\alpha s^{1/2})]. \tag{B.47}$$

The acoustic-cutoff frequency, ω_c, of the model ($D \geq s \geq 1$) is given by:

$$\omega_c = \frac{c_0\sqrt{m^2+1}}{2z_0}\frac{1}{\sqrt{s}}. \tag{B.48}$$

The model for this particular test is parametrized by $m = 1.5$, $z_0 = 768$ km, $D = 90.6198, c_0 = 8.51715$ km/s, $p_0 = 1.21 \times 10^5$ dynes/cm^2, $\rho_0 = 2.78 \times 10^{-7}$ g/cm^3, $H = z_0/(m+1)$ km, and $g = 0.1416$ km/s^2. Plotted in Figure B.6 are the analytical (dotted line) and the simulated (solid line) eigenfunctions. The sponge is placed adjacent to the upper boundary (located 1232 km above z_0), shown in Figure B.7. As can be seen the presence of the sponge does not affect the interior parts of the acoustic eigenfunction. There is an amplitude error near the upper-most region of the polytrope due to the combined influence of the boundary condition and the sponge but the nodes remain mostly unaffected.

A rough test of the efficacy of the boundary conditions is shown in Figure B.8, where an initial Gaussian-shaped velocity impulse is allowed to propagate outward. Panel a shows the situation at $t = 10$ min, and the successive panels show the impulses at later instants in time. The amplitude in panel d is of the order of 10^{-6}, significantly smaller than in panels a through c. Together with the test of Figure B.6, the boundary condition seems to allow outward propagating waves to leave the computational domain while leaving the eigenfunctions relatively undisturbed. A check of this sort was applied to choose the sponge for the real simulations (quite similar in magnitude and structure to the one in Fig. B.7). Since the polytrope + isothermal stratification near the surface is very similar to the model used in the simulations, and since the sponges are quite similar in structure, we expect that the eigenfunctions in the simulations are also well retrieved while the sponge damps the outward propagating waves.

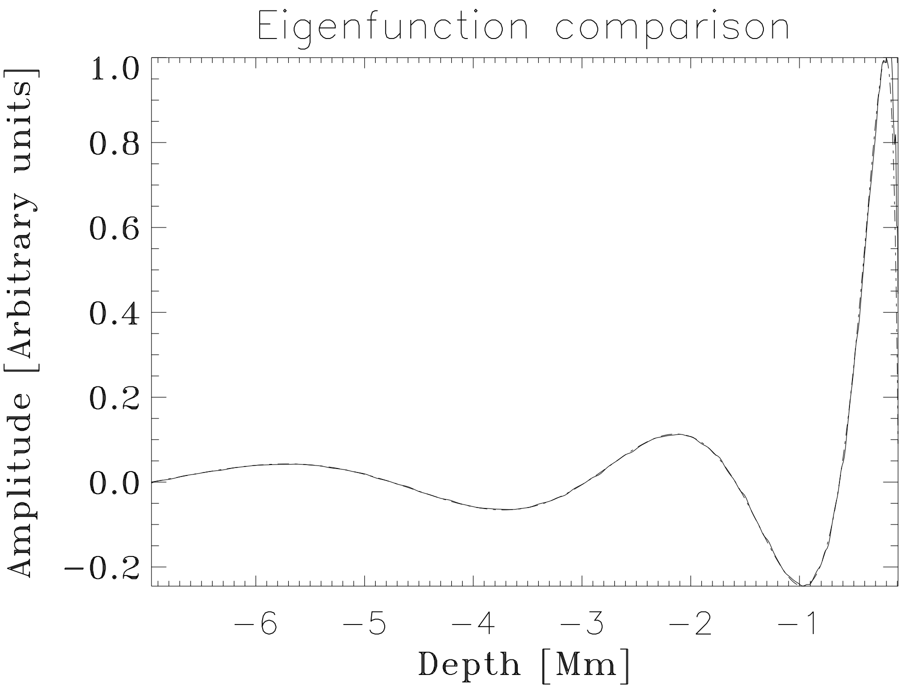

Figure B.6 Simulated (solid line) and analytical (dot-dash line) eigenfunctions for $\nu = 1.68$ mHz, for the model described above. It is seen that the boundary conditions and sponge do not affect the eigenfunction over the region of interest; although there is an amplitude error of a few % in the upper-most layers of the polytrope, the interior nodes are oblivious to the boundary conditions. This eigenfunction was obtained from a 24-hour simulation wherein the waves were constantly excited over a small region in the interior.

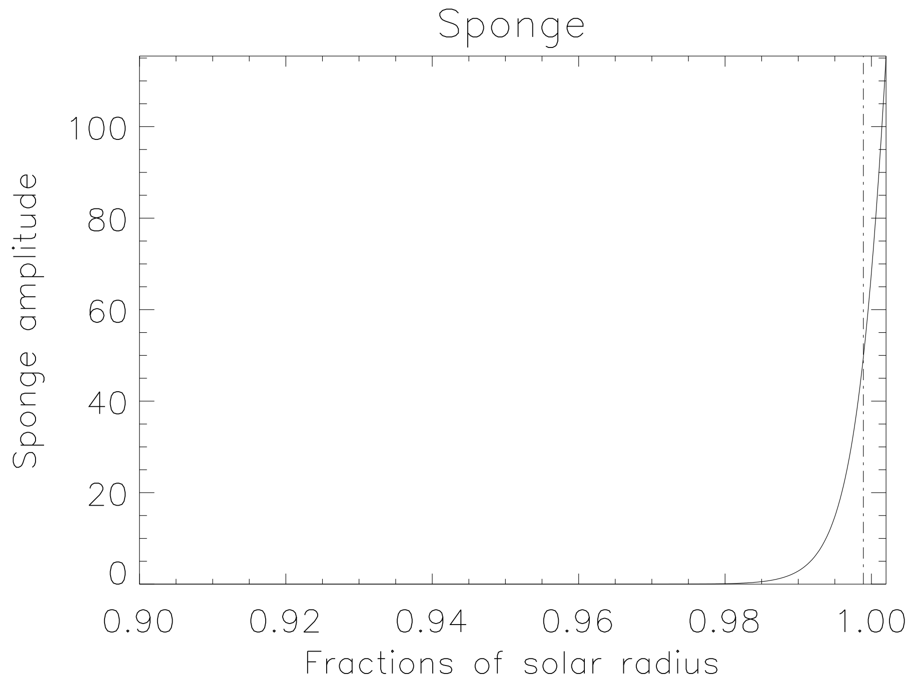

Figure B.7 The sponge (solid line) and the upper boundary of the polytrope (and lower boundary of the isothermal atmosphere) at $s = 1$ (dot-dash line). In simulations with the altered solar model, the sponge is slightly sharper (spatially) and pushed a little farther outward.

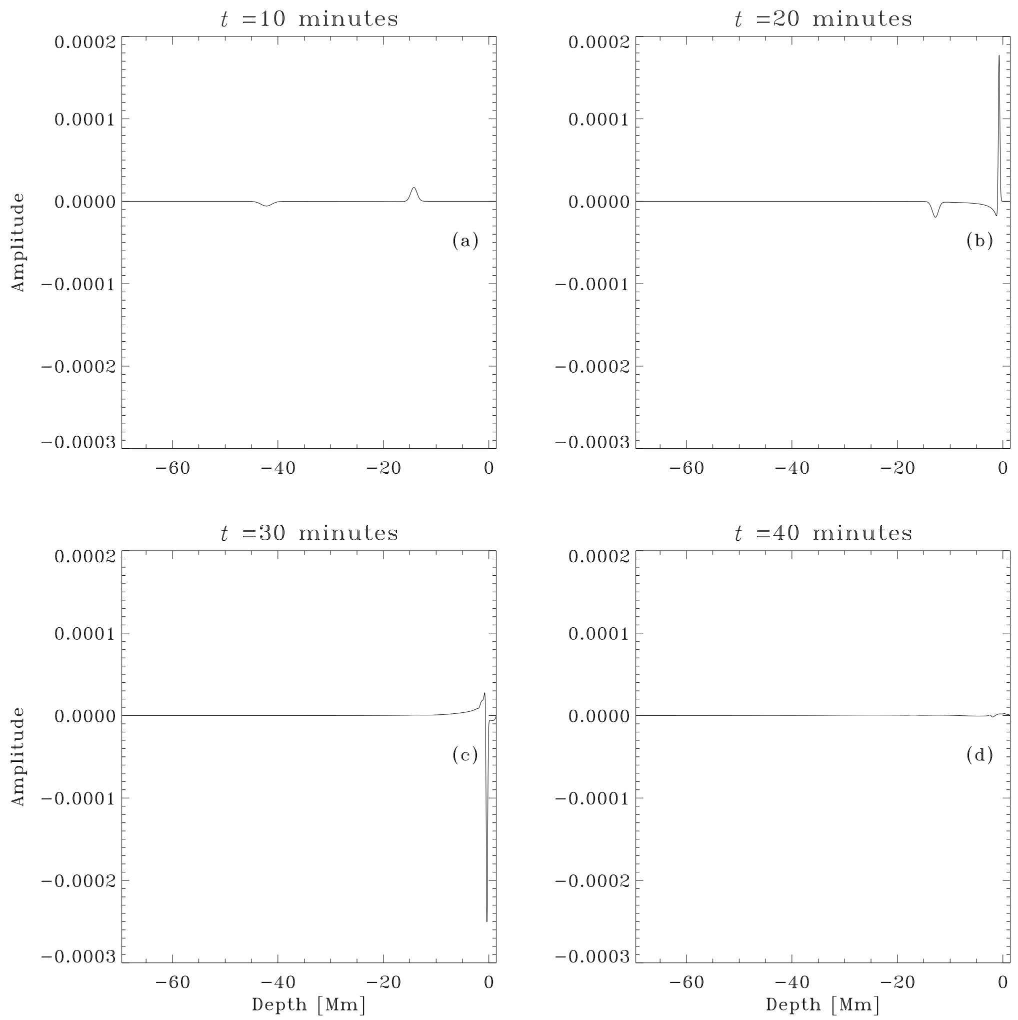

Figure B.8 Efficacy of the transmitting boundary. The initial condition is a Gaussian-shaped velocity impulse. Panel a shows the situation at $t = 10$ min, and the successive panels show the impulses at later instants in time. The amplitude in panel d is of the order of 10^{-6}, significantly smaller than in panels a through c. Together with the test of Figure B.6, the boundary seems to do a relatively good job of removing outward propagating waves while the interior portion of the eigenfunction is seen to be mostly undisturbed.

B.0.4 Spherical Harmonics and the optimized R-K scheme

Because analytical solutions in spherical geometry are difficult to come by, we constructed a simplified problem wherein wave propagation on the 2-D spherical surface (of radius $R = 1$) are studied. Provided background density, pressure are constant at all points on the surface, an analytical solution may be arrived at:

$$\begin{aligned} \partial_t \rho &= -\boldsymbol{\nabla} \cdot \mathbf{v}, && \text{(B.49)} \\ \partial_t \mathbf{v} &= -\boldsymbol{\nabla} p, && \text{(B.50)} \\ p &= \rho c^2, && \text{(B.51)} \end{aligned}$$

where the notation of the previous section applies here. The equations (B.49) to (B.51) are then simplified to obtain the following equations:

$$\begin{aligned} \partial_t^2 \rho - c^2 \nabla^2 \rho &= 0, && \text{(B.52)} \\ \rho(\theta, \phi, t = 0) &= \sum_0^{l_{max}} a_{lm} Y_l^m(\theta, \phi), && \text{(B.53)} \\ \rho(\theta, \phi, t) &= \sum_0^{l_{max}} a_{lm} Y_l^m(\theta, \phi) cos(\omega_{lm} t), && \text{(B.54)} \\ \omega_{lm} &= c\sqrt{l(l+1)}. && \text{(B.55)} \end{aligned}$$

Thus, the prescribed initial condition, first decomposed into the spherical-harmonic domain in equation (B.53), is evolved in time according to equation (B.54), where each spherical-harmonic coefficient oscillates at the frequency given by equation (B.55). Then, by choosing an initial condition that is completely captured by the spherical harmonics (in this case, $\rho(\theta, \phi, 0) = \cos\theta$), one can demonstrate the temporal error convergence rate, as shown in Figure B.9.

Finally, to show that spherical-harmonic error convergence turns exponential when a function is fully represented, we take the function $f(\theta, \phi) = \cos^{12}\theta \sin^6\phi$ and estimate the L_2 error in computing the latitudinal derivative $(-12\cos^{11}\theta \sin\theta \sin^6\phi)$ at various spherical-harmonic bandwidths (see Figure B.10).

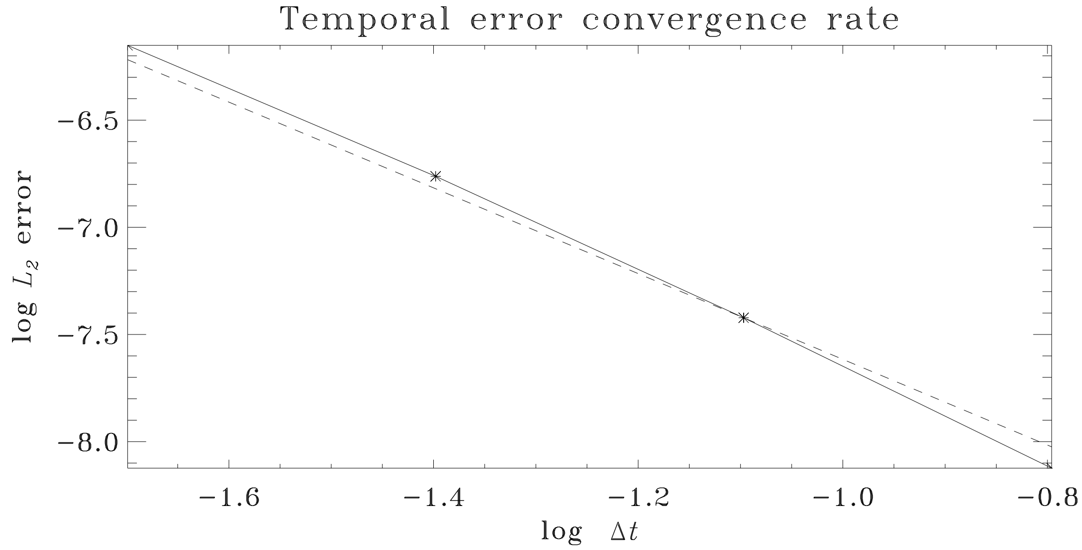

Figure B.9 Error convergence rate of the temporal scheme. The solid line is the error of the second-order five-stage scheme of Hu et al. (1996) and the dashed line is the theoretical second-order accuracy curve.

B.0.5 Measuring reflection phases

A concern with altering the background solar model is the extent of change in reflection phases and the size of the acoustic cavities. In order to measure the phases from simulations, we invoke Duvall's law (Duvall, 1982) which is an observational method to characterize the dispersion relation of the p modes. Because it is a difficult procedure to directly estimate the resonant frequencies from the simulations (requirements of temporally lengthy simulations), we use the frequencies produced by ADIPACK (Christensen-Dalsgaard & Berthomieu, 1991) as a proxy. Because ADIPACK has only a limited set of boundary condition options, the modes at higher frequencies which are more sensitive to the type of upper boundary condition are not represented well. We show in Figure B.11 that the modes with frequencies $\nu \lesssim 3.5$ mHz lie on the p-mode ridges while there are systematic errors at higher frequencies. Based on the results of (Duvall, 1982), we expect resonant modes of different n, l, and ω to collapse on to a single curve. A full theoretical treatment of this result may be found in (e.g.,

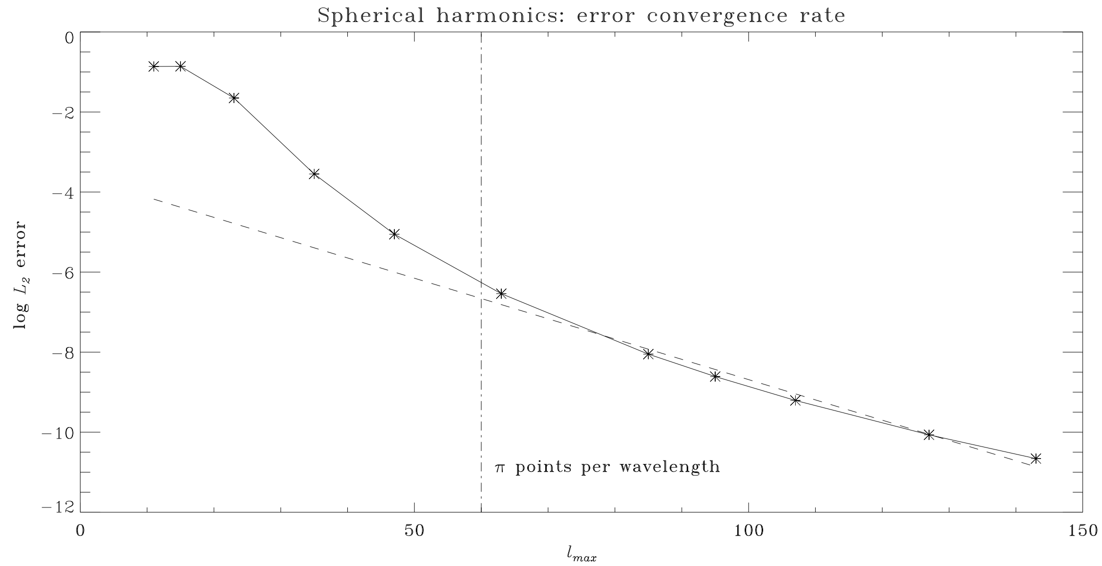

Figure B.10 Error convergence rate plotted against the spherical-harmonic bandwidth, l_{max}. The solid line displays the spherical-harmonic error in evaluating the latitudinal derivative and the dashed line shows the exponential convergence behaviour at high bandwidth. The onset of exponential convergence in the case of (sine/cosine) Fourier series occurs when the grid resolution reaches approximately π points per wavelength. We expect a similar effect to apply to the spherical harmonic basis. Since the number of latitudes n_{lat} must satisfy $n_{lat} \geq l_{max}$, and because $l_{max} = 19$ is sufficient to capture the function $-12\cos^{11}\theta\sin\theta\sin^6\phi$, we expect the onset of exponential convergence to occur at $n_{lat} = l_{max} \sim 60$. The vertical dot-dash line indicates this location in the figure.

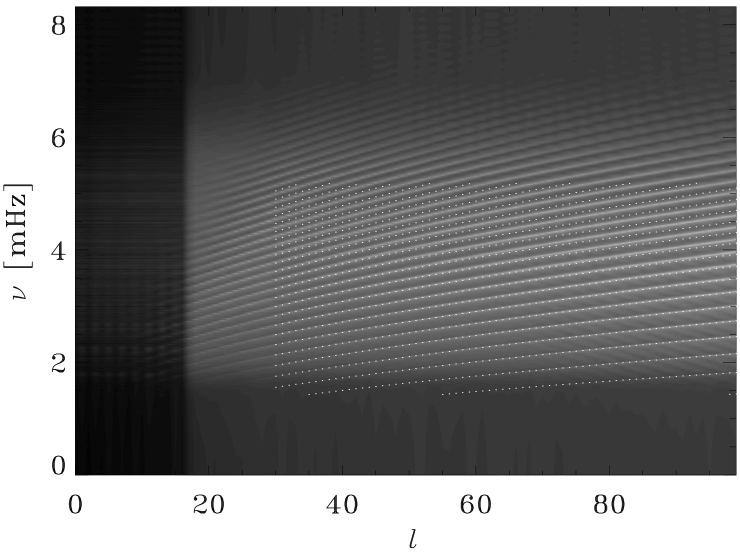

Figure B.11 Power spectrum from a simulation. The dots show frequencies as estimated by ADIPACK (Christensen-Dalsgaard & Berthomieu, 1991). At lower frequencies, we observe a good match between the predicted and simulated dispersion relations, while the agreement is not quite so good at higher frequencies.

Christensen-Dalsgaard, 2003). In Figure B.12 b, we see that indeed, the modes do collapse onto a curve, but with a reflection-phase constant α of 1.05, as compared to $\alpha = 1.13$ for the solar frequencies (panel a). The value of α in the solar case was chosen to minimize the spread between a fifth-order polynomial fit (the dot-dashed line in Figure B.12 a) to the frequencies; it appears that altering the solar model has changed the size of the acoustic cavity and shifted reflection phases to the tune of 0.08 radians or about 4.58°, contributing to a 7% error per reflection. These phase shifts result in systematic changes in the travel times of the p modes, as shown in Figure B.13 (private communication, Olga Burtseva and Shukur Kholikov). The error is small enough that conclusions drawn from these differential studies are probably valid.

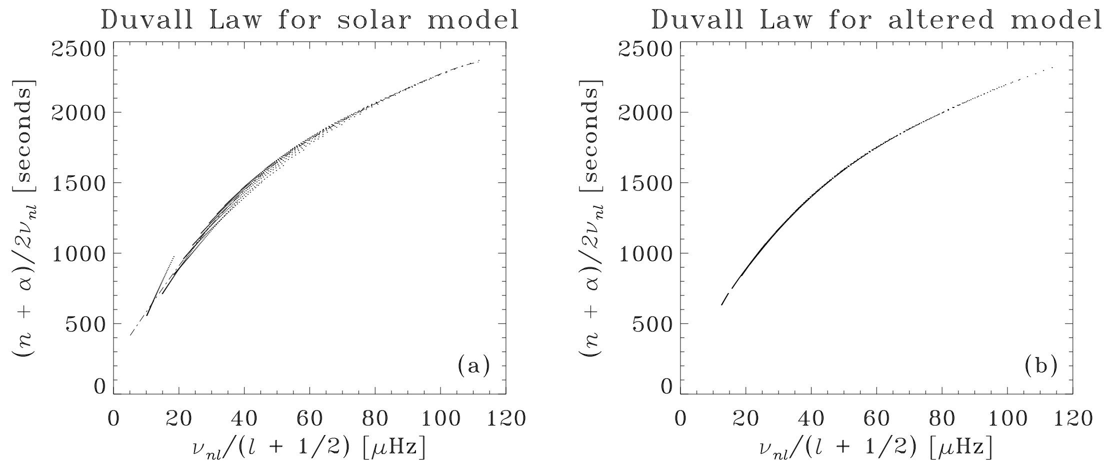

Figure B.12 Duvall's Law (Duvall, 1982) for a solar model (panel a) and the altered model (panel b). Resonant modes (obtained using ADIPACK) of the artificial model used in the simulations collapse onto a single curve as seen in b. $\alpha = 1.05$, minimizes the spread in the altered model, while $\alpha = 1.13$ is the optimal value for the solar frequencies (panel a). The spread in panel a is defined relative to a fifth-order polynomial fit (dot-dash line) to the solar frequencies. The error in the reflection phase is 7%.

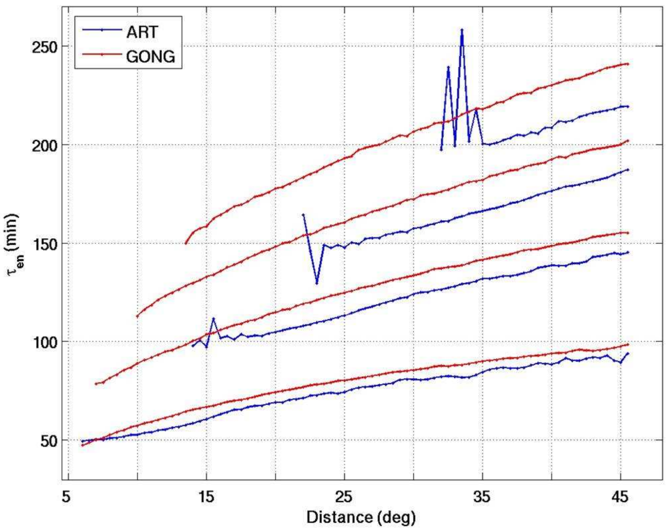

Figure B.13 Envelope (group) travel times for differing numbers of bounces; simulated or artificial data (ART) and GONG data (GONG). Due to the altered solar model, a systematic difference between the travel times associated with real and artificial data is observed. In each of the comparisons, the modes of the simulated data possess lower travel times (private communication, Olga Burtseva and Shukur Kholikov).